Investigation of the flow redistribution upstream of grid-like obstacles separated by a variable gap

Jérome Cardolaccia, Stanislas de Lambert

Investigation of the flow redistribution upstream of grid-like obstacles separated by a variable gap

Jerome Cardolaccia[1], Stanislas de Lambert[1]

Abstract

In nuclear Pressurized Water Reactors, fuel assemblies are slender structures composed of many rods held together by regularly spaced grids. Intense in-core conditions may sometimes result in permanent deformations impairing the reactor normal operation or even challenging its safety. Fluid-structure interactions are the central plot of this multiphysical storyline, and the water gaps between adjacent fuel assemblies act as the main character. More specifically, the flow redistribution upstream of grids, from the water gap to the rod bundle or the other way around, affects the force which is exerted by the coolant on the grids. Analytical models accounting for this effect can be found in the literature. The present article describes a simple experiment dedicated to providing validation data to such models. Mock-up grids were 3D printed and disposed in a hydraulic loop with a variable distance between them. For each configuration, the mean axial velocity was probed at hundreds of locations inside the water gap using an LDA acquisition system. The flow rate was then computed with several methods compensating the lack of velocity measures in unreachable areas. This experimental campaign helped to gain insight into the flow behavior across the grids of a fuel assembly. Notably, near proportionality was demonstrated between the water gap width and the flow rate through it. It was also observed that the redistribution cross-flows take place in a very limited region upstream of the grids.

Highlights

- Mock-up grids were 3D-printed, with hydraulic features similar to nuclear fuel grids'
- Two such grids were mounted in a water loop with an adjustable gap between them
- LDA was used to measure the axial velocity at numerous locations inside the gap
- Different methods were benchmarked to obtain the flow rate from the LDA measures
- Near proportionality was observed between the flow rate and the gap width

Declarations

Funding: 100% CEA (as our employer)

Conflicts of interest/Competing interests: None

Availability of data and material: Figshare (see references)

Code availability: Available upon request

Authors' contributions: All authors contributed to the study conception and design. Material preparation, data collection and analysis were performed by Cardolaccia J. The first draft of the manuscript was written by Cardolaccia J and all authors commented on previous versions of the manuscript. All authors read and approved the final manuscript.

[1] *Université Paris-Saclay, CEA, Service d'études mécaniques et thermiques, 91191, Gif-sur-Yvette, France*

List of symbols

$\boldsymbol{A}$	Cross-sectional area of the test section (m^2)
$\boldsymbol{A_B}$	Cross-sectional area inside the bypass $= \boldsymbol{L_Y}\bar{\boldsymbol{\lambda}}$ (m^2)
$\boldsymbol{A_G}$	Cross-sectional area inside both half-grids (m^2)
$\boldsymbol{A_W}$	Cross-sectional area of the washbowl (m^2)
$\boldsymbol{f}$	Darcy friction factor
$\boldsymbol{h}$	Height of the grid bevel (m)
$\boldsymbol{K_G}$	Pressure loss coefficient of the mock-up
$\boldsymbol{L_X}$ $\boldsymbol{L_Y}$ $\boldsymbol{L_Z}$	Dimensions of one individual holed plate (m)
$\mathbf{PF}$	Profile Factor defined by $\boldsymbol{w_B^{max}/w_B}$ $(> \mathbf{1})$
$\boldsymbol{Q}$	Flow rate of the hydraulic loop (m^3/s)
$\boldsymbol{Q_B}$	Flow rate through the bypass between grids (m^3/s)
$\boldsymbol{Q_G}$	Flow rate through the holes of the grids (m^3/s)
$\boldsymbol{q_i}$	Flow rate per unit length in the bypass for the $\boldsymbol{i}$-th row of LDA measures parallel to $\boldsymbol{X}$-axis (m^3/s)
$\mathbf{Re_B}$	Reynolds number based on $\boldsymbol{\lambda}$ and $\boldsymbol{w_B}$
$\mathbf{Re_G}$	Reynolds number based on $\boldsymbol{\phi}$ and $\boldsymbol{w_G}$
$\boldsymbol{w}$	$\boldsymbol{Z}$-component of local time-averaged velocity measured by LDA (m/s)
$\widehat{\boldsymbol{w}}_{\boldsymbol{i}}$	[function of $\boldsymbol{x}$] Approximate profile of $\boldsymbol{w}$ along the $\boldsymbol{i}$-th row of LDA measures parallel to $\boldsymbol{X}$-axis (m/s)
$\boldsymbol{w_B}$	Bulk velocity through the bypass (m/s)
$\boldsymbol{w_B^{max}}$	Centerline (= maximum) velocity in the bypass (m/s)
$\boldsymbol{w_G}$	Bulk velocity though the grids (m/s)
$\boldsymbol{x}$ $\boldsymbol{y}$ $\boldsymbol{z}$	Coordinates along $\boldsymbol{X}$-, $\boldsymbol{Y}$- and $\boldsymbol{Z}$-axis respectively (m)
$\boldsymbol{\Delta p}$	Pressure drop measure (Pa)
$\widehat{\boldsymbol{\Delta p}}$	Reconstruction of pressure drop from other available measures (Pa)
$\boldsymbol{\Delta z}$	Rise of the free surface when measuring $\boldsymbol{A_G}$ (m)
$\boldsymbol{\varepsilon}$	Wall roughness of 3D-printed parts (m)
$\boldsymbol{\theta}$	Blockage ratio of the grids
$\boldsymbol{\lambda}$	Bypass width (m)
$\bar{\boldsymbol{\lambda}}$	Average of the $\mathbf{10}$ gauge block measures of $\boldsymbol{\lambda}$ (m)
$\boldsymbol{\rho}$	Water density (kg/m^3)
$\boldsymbol{\varphi}$	Angle between the bevel and the $\boldsymbol{Z}$-axis (rad)
$\boldsymbol{\phi}$	Mean diameter of the grid holes (m)

1 Context and literature review

In Pressurized Water Reactors (PWR), the heat generated by the fission of uranium and plutonium nuclei is transported by the liquid water flowing through the nuclear core, made up of fuel assemblies (FA). In the French power plants (Coppolani et al. 2004), these FA are made of 264 cylindrical fuel rods bundled together around a rigid skeleton consisting of ten or so spacer grids distributed regularly along 25 guide tubes. The spacer grids are designed to maintain a regular pitch of about 1 cm in the 17-by-17 square array of fuel rods. FA are slender structures submitted to extreme conditions in terms of temperature, irradiation and mechanical/hydraulic loading. Consequently, they can be very prone to lateral deflection.

Accounts of FA which were deformed during their presence in the reactor have been publicly reported on a regular basis since first observation in the 1990's (*e.g.* Andersson et al. 2005; Fetterman et al. 2008; IAEA 2010; IRSN 2012; IRSN 2017; Gabrielsson et al. 2018). The bowing of FA has repercussions in terms of safety during both maintenance and operational conditions. At the end of an operating cycle, FA are maneuvered to be either unloaded out of the core or rearranged to another location. The insertion or extraction of bowed FA can be tedious work, delaying the outage schedule (with financial prejudice) or, rarely, causing damage to some spacer grids. In the worst case, some fragments might be torn off the grids and impact or wear the rods cladding later when the water is recirculated. During operation, the distortion of the core geometry induced locally by FA bowing have immediate effects on the hydraulic, heat and neutronic balances. It is thought that these local perturbations might in some scenarios propagate to a larger region of the core, reducing considerably the operational margins and leading to supplementary burnup in a couple of the FA. In a few occurrences, heavily tilted power distribution could be attributed to collective assembly bow. Last but not least, lateral deformations may slow down the drop of the control rods or even lead to incomplete rod insertion.

Several models meant to estimate FA bowing have been published (*e.g.* Karlsson and Manngård 1999, Stabel et al. 2011, Horváth and Dressel 2013, Lascar et al. 2015, Wanninger et al. 2018, de Lambert et al. 2020). Some of them claim good *a posteriori* agreement with experimental or industrial measures

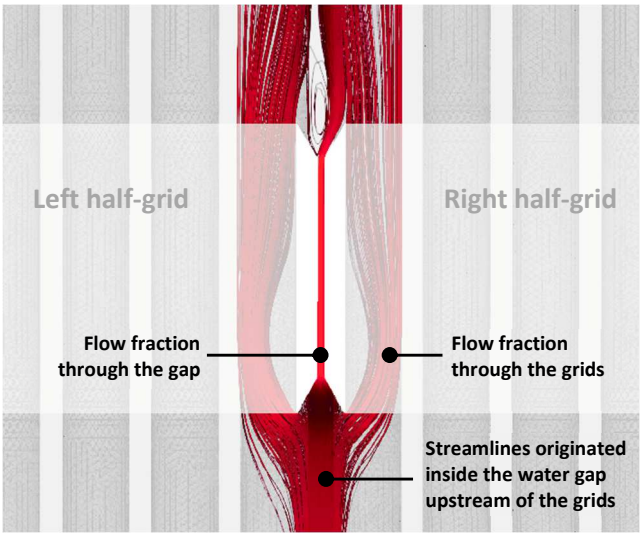

Fig. 1 Flow redistribution upstream of porous grids separated by a 1 mm gap (CFD screenshot adapted from de Lambert et al. 2020)

of the deflection. The physical phenomena generating lateral deflections in PWR cores are globally

identified; yet, we still lack of a comprehensive and efficient numerical model to predict them for routine scenarios: normal operation over a full cycle, new core loading pattern, pump malfunction, grid design modification... This may originate from the complex entanglements between the thermal, hydraulical, mechanical and neutronical mechanisms at stake. Among the leading causes of FA bowing, the hydraulic loadings applied by the coolant's substantial flow rate is maybe one of the most elusive. Water flows through the core at an average velocity around 5 m/s, which would be enough to lift the FA if they were not held down tightly at their top. The resulting state of compression favors lateral bending in itself. Additionally, large-scale cross-flows appear near the inlet and outlet of the core in order to counteract against the inhomogeneous flow rates feeding FA in the center or outer regions of the core (Fournier et al. 2007, Karoutas et al. 2010, Xu et al. 2012). Such lateral flows through tube bundles obviously yield a lateral force on them. At last, the pressure difference across both external faces of a spacer grid is another significant source of lateral effort on the FA.

This latter effect has been particularly studied by Ricciardi and Boccaccio (2015), whose simple analytical model accounted for the variation of each water gap – also called "bypass" – surrounding an oscillating FA, in order to assess the lateral force on its grids. De Lambert et al. (2020) then provided a more detailed analytical model of the flow behavior through the thin bypass between two adjacent grids. In that paper, the authors explain how the fluid goes preferentially through the bypass or through the grids according to the distance between them (see Fig. 1). Their model is able to predict the pressure drop as well as the flow rate distribution when this distance changes. In the present paper, we offer to provide experimental data to support their theoretical work. To the best of our knowledge, no other authors working on FA bowing focused on modeling the water gap to that degree.

2 Experimental setup

In order to investigate how the flow distribution changes when two adjacent grids are brought closer and closer, we designed a generic mock-up of spacer grid. We needed not to reproduce all the details of real spacer grids such as springs, dimples or mixing vanes (see Coppolani et al. 2004 for a thorough description), because almost every available model of FA bowing uses a homogeneous approach to represent the fluid behavior (often a porous medium or a hydraulic network). Instead, we just wanted the mock-up grid to act like a "pressure drop" device as spatially uniform as possible, yet keeping the essential features of the real grids: no cross-flows internal to the mock-up grid (axial flow only), fidelity to the bypass geometry (with guide vanes at the inlet and outlet), pressure drop coefficient not far from unity. For the same reasons, the presence of rod bundles mimicking actual fuel assemblies is not required: they affect ever so slightly the flow redistribution phenomenon (adding very little complexity to the numerical models) but would demand tremendous experimental effort to be properly accounted for.

In the end, the mock-up *half*-grid was 3D printed in polyethylene terephthalate (PET) plastic material with a Volumic Stream 30 Ultra printer. The accuracy of the 3D-printing process is poor compared to

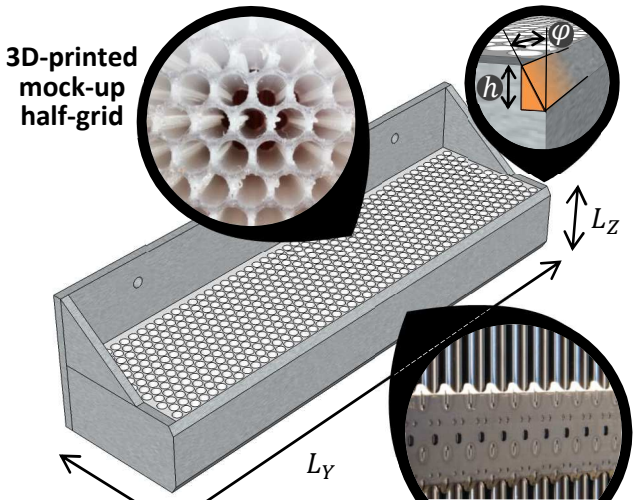

Fig. 2 Overview of the mock-up half-grid and close view of the actual 3D-printed device; the beveled edge mimics the outer strap of an actual grid (example reproduced from Framatome 2018)

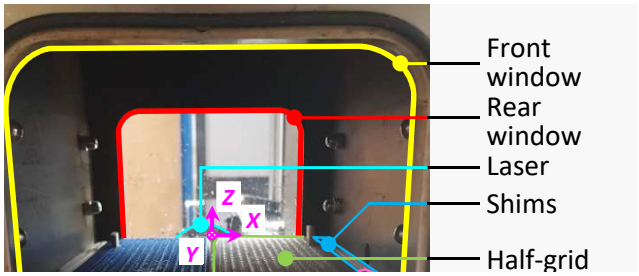

Fig. 3 Description of the experimental mock-up named DIVA+G

standard stainless steel machining; however, geometrical imperfections are hardly a nuisance in our case and production costs were more than 100 times cheaper. An overview of the printed mock-up is visible on Fig. 2. Its main part is a plate (4 cm thick) with 618 circular through-holes (5.2 mm in diameter) arranged in a triangular array (6 mm of pitch). Another plate was created perpendicular to its base for ensuring a rigid fixation to the wall of the hydraulic loop thanks to a screw-nut system. Small triangular-shaped stiffeners were added at the T-junction of the plates. All these parts were printed in one single pass and are fully filled so as to minimize the mock-up deformation under flow.

Two of such half-grids were printed and placed in the test section of a hydraulic loop, of cross dimensions 18×30 cm^2. Centimeter-thick fillers were appended to both half-grids to block water from flowing in the remaining gap between them and the acrylic windows (hence mitigating the boundary effects). A set of shims was crafted from stainless steel sheets of various thicknesses between 0.5 and 3 mm, with holes drilled at the locations of the screw-nut fixations. These shims allowed to adjust the distance between the two half-grids. The water gap width could thus be varied from 0 to 20 mm. The whole setup described above will be referred to as DIVA+G from here on (Fig. 3).

A pump circulated water in the test loop at near atmospheric conditions. During all the tests, the flow rate was maintained at 120 L/s and the temperature was stabilized at 20°C (Reynolds number around $5\ 10^5$ in the empty test section). A mixing device (not visible on Fig. 3) and a filtration grid ensured spatially uniform inlet conditions at the bottom. There was approximately 20 cm both upstream and downstream of the mock-up, which is enough not to disrupt the redistribution phenomenon at stake in this article.

Two small pressure taps were situated in the solid wall, below and above one of the half-grids. They were connected to a Validyne differential transducer (DP15-42), whose calibration allowed to measure the average pressure drop (no hydrostatic component) with an uncertainty of $\pm 5\%$.

The mean velocity was probed inside the water gap thanks to a Laser Doppler Anemometry (LDA) commercial equipment (Dantec FlowLite). The impurities naturally present in water made additional seeding unnecessary (we checked that the flow rate measured from LDA matched the

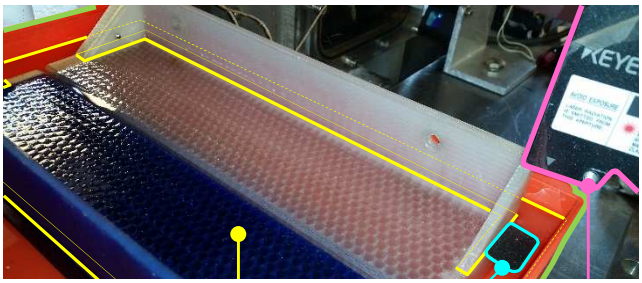

Fig. 4 Indirect measure of the cross-sectional area of the grids

flowmeter output). A HeNe laser of 10 mW was associated to a long-focal lens (310 mm) so that the full depth of the test section could be reached. The tradeoff is that the probe volume was elongated (2.4 mm) in the Y direction, which is hardly a problem since the flow is somewhat spanwise invariant between the grids. The use of a Bragg cell allowed to distinguish the flow direction. An automated 3-axis traverse system (with 0.1 mm resolution) displaced the probe volume to the hundreds of locations required to cover all the required cross-section. Each location was held until 500 bursts were validated or the 20-second timeout was expired. The velocity measurement uncertainty was found to be far below 1% in air with a rotating disk. During the repeatability tests in the empty loop, the 500-burst threshold was not reached everywhere near the rear window when the width of the bypass was under about 5 mm. In such conditions, statistical uncertainty adds up to LDA intrinsic uncertainty. The statistical moments were weighted by the particles travel times to correct a slight bias inherent to the LDA technique (McLaughlin and Tiederman 1973), which would lead to an overestimation of the mean velocity by about 1% in our case if uncorrected.

Our raw measures (LDA, differential pressure, block gauges) and post-processings are available on *Figshare* for anyone to download and to use (see references).

3 Half-grids cross-sectional area and pressure drop coefficient

The grid features strongly affect the flow redistribution to or from the water gap. For instance, the more opaque the grids are, the larger the flow rate is in the water gap. The opacity is defined from the cross-sectional area of the grids – that is the sum of the areas of its through-holes. The actual value is quite different from the design value because of warping and shrinkage inherent to the 3D printing process by Fused Deposition Modeling (FDM). No attempt was made at improving the printing process; instead, we devoted our time to measuring accurately the real cross-sectional area A_G and pressure loss coefficient K_G of the half-grids.

The cross-sectional area A_G was determined by immerging the printed parts in a washbowl so that the free surface was flush with the top end of the through-holes (Fig. 4). The consequent rise Δz of the free surface was captured by a Keyence laser displacement sensor. The cross-sectional area A_G could then be deduced from Eq. (1):

$$A_G = 2L_X L_Y - \frac{1}{L_Z}(2L_Y h^2 \tan(\varphi) + A_W \Delta z) \qquad (1)$$

where L_X, L_Y and L_Z are the dimensions of the holed plate of one individual half-grid, h is the height of the bevel and φ its angle with respect to the vertical Z-axis (see Fig. 2), A_W is the cross-sectional area of the washbowl. We found $A_G = 245.0$ cm^2 with an uncertainty around 10 cm^2. Over one third of the uncertainty is explained by the presence of the counter-nuts in 16 of the 1236 holes; another third accounts for the difficulty of assessing accurately the free surface leveling; about the last third directly comes out of the uncertainties on the measures of L_X and L_Z.

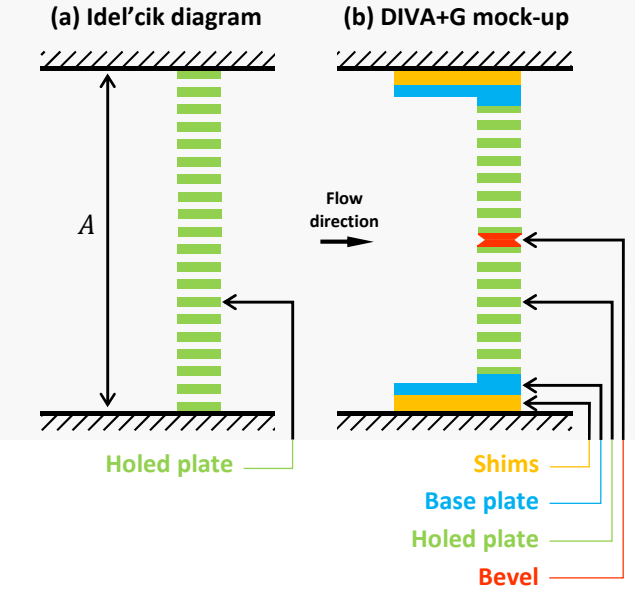

Fig. 7 Comparison of Idel'Cik's thickened perforated plate and actual mock-up geometry

That value of A_G corresponds to a mean hole diameter of around $\phi = 5.0 \pm 0.1$ mm. As said earlier, this is less than the design value (5.2 mm), but the ratio is consistent with the shrinkage observed macroscopically on L_X, L_Y and L_Z. As a consequence, the pressure drop coefficient K_G would also differ from the predicted value but, again, this was not a problem as long as we were able to measure it precisely.

In order to determine K_G, we added 13 mm of shims on each side of the mock-up so as to close the water gap completely. Hot-melt glue was applied to seal it properly. Then, the pressure drop Δp was measured for several values of the flow rate Q and the coefficient was inferred by linear regression according to Eq. (2) below:

$$K_G \overset{\text{def}}{=} \frac{\Delta p A^2}{\frac{1}{2}\rho Q^2} \tag{2}$$

where ρ is the water density and A is the cross-sectional area of the empty test section.

Fig. 5 gives $K_G = 4.25$ in the case of a fully closed gap, with an uncertainty of $\pm 3\%$ (due to propagation of uncertainties on Δp and Q measurements). This is higher than in an actual PWR (around 1), but does not hinder our approach regarding the validation of semi-empirical models (for which K_G is merely an input parameter).

A simple *a posteriori* model for the value of K_G can be built from the correlations for thickened perforated plates found in Idel'cik (1986), diagram 8-4 :

$$K_G = \left(\zeta_\varphi + (1-\theta)\left(\frac{3}{2} - \theta\right)\bar{\varepsilon}_0^{\mathrm{Re}} + \frac{f L_z}{\phi}\right)\frac{1}{\theta^2} \tag{3}$$

Idel'Cik's correlation above contains two coefficients which are linearly interpolated from tables, namely $\zeta_\varphi = 0.027$ and $\bar{\varepsilon}_0^{\mathrm{Re}} = 0.82$. The value of K_G primarily depends on the blockage ratio θ, which is the ratio of the cross-section A_G inside the grids over the cross-section "upstream of the obstacle". Fig. 7b shows that the perforated part in the mock-up

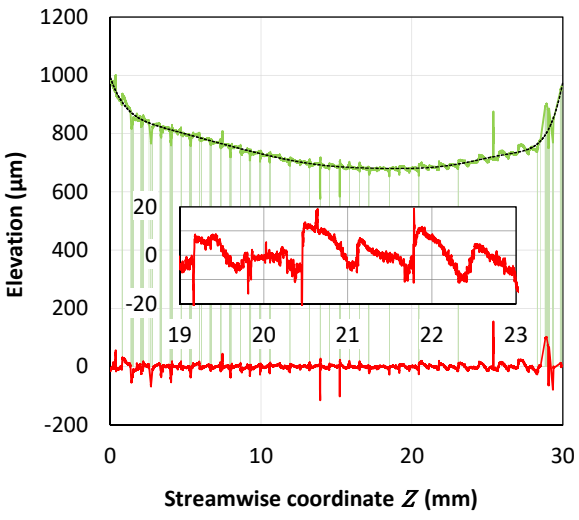

Fig. 6 Roughness profile along a through-hole measured in a partially printed grid (— Raw profile with measure artifacts; ------ Large-scale polynomial trend; — Detrended profile)

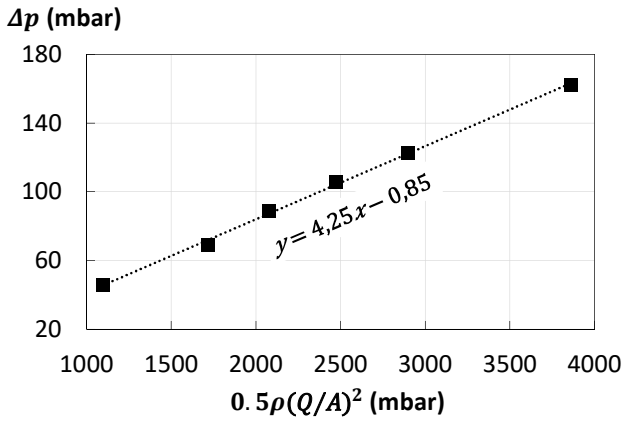

Fig. 5 Linear regression for the determination of the pressure drop coefficient K_G when the gap is fully closed (■ Experimental measures; ····· Linear regression)

(green) is restricted by the base plate and a various number of shims (blue and yellow). When the gap is closed, the holed plate occupies only 80% of the whole test section $A = 540$ cm^2. The pressure drop will clearly be higher in the actual configuration of Fig. 7b compared to the configuration given by Idel'Cik where there are no shims nor base plate (Fig. 7a). We thus use the full $A = 540$ cm^2 as the upstream area, which gives $\theta = A_G/A = 0.45$. This is equivalent to using a grid without shims nor base plate as in Fig. 7a, with holes of same diameter $\phi = 5$ mm as in the actual mock-up (Fig. 7b) but with a larger pitch between them. The wall roughness ε is the last important parameter of Idel'Cik's formula, because Darcy's friction factor f strongly depends on it, using *e.g.* Haaland's Eq. (4):

$$f = \left(-1.8\log_{10}\left(\frac{6.9}{\mathrm{Re}_G} + \left(\frac{\varepsilon}{3.7\phi}\right)^{1.11}\right)\right)^{-2} \qquad (4)$$

We measured ε within the holes of a partly printed item thanks to a laser optical profilometer. Profiles measured along the Z-axis (*ie* in the streamwise direction), at the bottom of one hole, revealed several possible scales for the roughness ε (Fig. 6):

- Intrinsic PET material roughness is typically around 1 µm (detrended arithmetical mean deviation).
- Additionally, artifacts were observed regularly spaced along the Z-profile. They precisely demarcate between different parts of the wire deposed at 45° in the XZ-plane, half parallel and half transverse to the flow (the printed layers were piled up along the Y-axis). The Z-profile thus exhibits about 60 irregular hills all the way through the hole, with steep cliffs up to 30 µm of elevation.
- If we zoom out even further, the general landscape is a valley (the middle of the through-hole) sunk nearly 200 µm below two mountains (both ends of the through-hole). Such a deflection may not exist in the fully printed items which were actually mounted in the hydraulic loop.

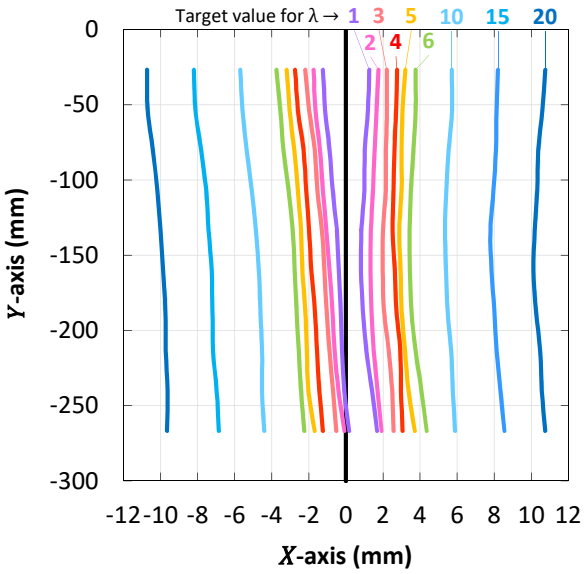

Fig. 8 Reconstruction of the water gap geometry from the combination of gauge block and LDA measures

If we set $\varepsilon = 30$ µm, Eq. (3) yields exactly $K_G = 4.25$ by using the lower bound of the uncertainty range for A_G (*ie* $\phi = 4.9$ mm and $\theta = 0.44$). This validates the use of Idel'Cik's correlation to assess the value of K_G.

As a corollary, we must acknowledge that the value of K_G depends significantly on the gap width λ. Indeed, A represents the channel cross-section upstream of the grids, with the gap sealed and the width of the shims included. Therefore, every time that shims are removed, the value of A decreases accordingly. In concrete terms, we now have $\theta = A_G/(A - A_B)$ in Eq. (3). Following this logic, we calculated the values of K_G given by Idel'Cik's correlation for λ varying from 0 to 20 mm. The linear regression in Eq. (5) provides an excellent approximation of the results (λ must be provided in millimeters):

$$K_G(\lambda) = 4.23 - 0.06\lambda \qquad (5)$$

4 Pressure drop and flow rates as a function of the gap width

The water flow can cross the grids level by going either through the holed plates or through the bypass between them. The fraction of the stream which goes either way depends mainly on the gap width and the pressure drop coefficient of the grids (de Lambert et al. 2020). The pressure drop

coefficient K_G has been determined in section 3. The gap width was measured whenever shims were added or removed, with gauge blocks down to a tenth of millimeter, at ten positions steadily spaced along the Y-axis. The mean gap width, noted $\bar{\lambda}$, was consistently about half a millimeter larger than expected for all the tested configurations (target values between $\lambda = 1$ and $\lambda = 20$ mm). This discrepancy is mainly explained by the mock-up geometrical distortions related to the 3D-printing process. Fig. 8 shows the water gap reconstructed from the gauge block measures (for the gap width) and the LDA measures (for the position of the gap along the X-axis). The wall shape is very similar for all values of λ, indeed revealing the half-grids irregularities. Small variations between configurations can be attributed to differences in the clamping force and to uncertainties in the measure with the gauge blocks. The geometrical imperfections visible in Fig. 8 may very slightly impair the flow homogeneity along the Y-axis. Nevertheless, the relative standard deviation around $\bar{\lambda}$ reaches only 30% at most (for the smallest bypass: $\bar{\lambda} = 1.6$ mm) and we had good faith that it would make no noticeable difference in terms of flow rates and pressure drop, compared to an hypothetic straight water gap. Anyway, such details are not reproducible in theoretical models, which generally take the average distance $\bar{\lambda}$ as the only input for the bypass geometry. Later in this article, we provide insight into how our experimental results compare with the analytical model of de Lambert et al. (2020), advocating our choice not to strive for enhancing the 3D-printing output quality.

Even though the mock-up deformation did not perturb the flow homogeneity, it still made the LDA measures troublesome for small water gaps. Indeed, the far end of the test section was not accessible to the laser probe when $\lambda = 1$ mm, for obvious optical reasons (Fig. 8). Moreover, due to the probe dimensions, the velocity decrease down to zero at the walls could not be captured, whatever the gap width. Therefore, the computation of the flow rate from the local measures of axial mean velocity was not so straightforward *a priori*. In order to challenge the trivial integration strategy (noted M0 thereafter), we developed two methods aimed at reconstructing the velocity signal where the probe was unable to go, namely close to the walls and, for small values of λ, near the rear window (see Fig. 9a and 9b).

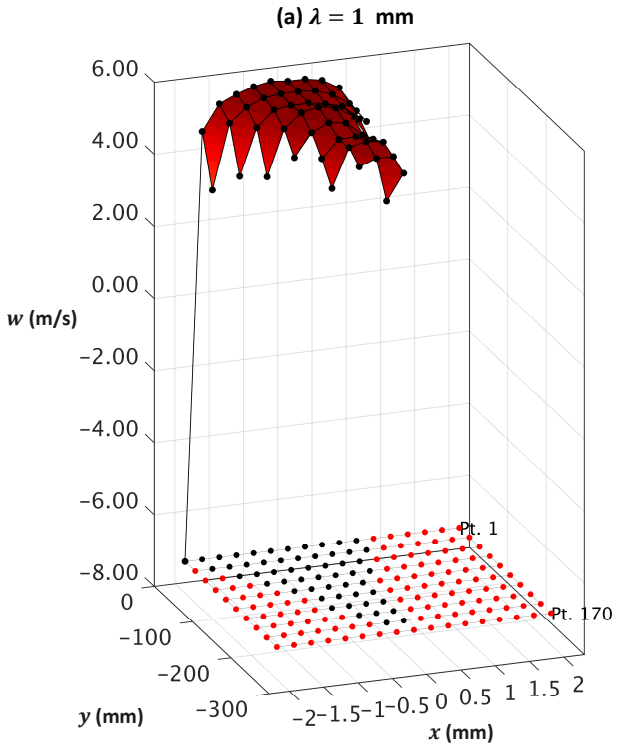

Fig. 9 LDA measures for **(a)** the thinnest gap and **(b)** the widest gap; the path followed by the laser probe is visible below the mean velocity 3D profiles; red points are locations where not a single burst was validated.

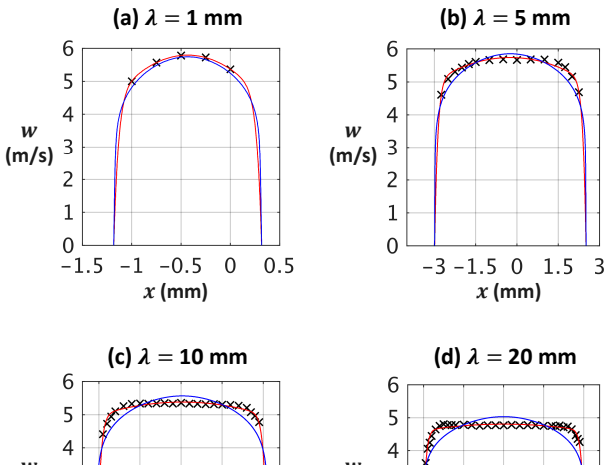

Fig. 10 Typical velocity profiles in the water gap for various gap widths λ (× Experimental measures; — Experimental data fit [method M2b]; — Fully developed profile [CFD results])

The first method (labeled M1) assimilates the water gap to a plane channel flow, invariant along the Y-axis. Provided that the flow is fully developed, the axial mean velocity is thus reduced to a 2D profile (in the XZ-plane) characterized by the sole Reynolds number. The idea then leans on the fact that, in such a situation, an empirical relationship exists between the centerline velocity and the bulk velocity, and that the former is much easier to measure experimentally than the latter:

- The ratio of centerline $w_B^{\max}$ to bulk velocity w_B (so-called Profile Factor PF) can for instance be evaluated by Dean's correlation (Dean, 1978):

$$\mathrm{PF} = 1.28\,\mathrm{Re}_B^{-0.0116}\ ;\ \mathrm{Re}_B \in \left[6\,10^3; 6\,10^5\right] \qquad (6)$$

- We found that the third quartile of the LDA data is a good estimator for the centerline velocity $w_B^{\max}$ whatever the gap width λ.

The bulk velocity w_B is obtained after some fixed-point iterations (since Re_B itself depends on w_B). Finally, the flow rate in the water gap Q_B is expressed as the product of the bulk velocity w_B and the cross-sectional area $A_B = L_Y\bar{\lambda}$.

The main drawback of method M1 is that the channel flow is hardly ever fully developed in our

tests. The entrance length in turbulent duct flows is not easy to assess; Anselmet et al. (2009) state that significant discrepancies exist in the literature regarding its value. Moreover, it notoriously depends on the aspect ratio of the channel section and the inlet geometrical conditions. Several correlations giving the entrance length are benchmarked by the authors, all of which indicating that the bypass is not long enough in our tests, except possibly for the thinnest gap ($\lambda = 1$ mm). This is clearly confirmed by Fig. 10 which compares our experimental data (black crosses with red fitting curve) versus CFD-computed fully developed channel flow profiles at the same Reynolds number (blue curve). The blue numerical curves were obtained with code Cast3M, using the Spalart-Allmaras turbulence model. Smooth walls were considered in the simulations.

In summary, method M1 computes the flow rate Q_B with very little uncertainty for large gaps ($\pm 2\%$) because lots of data is available to assess the centerline velocity; however, a systematic bias error (underestimation down to -5% according to Fig. 10) is committed by wrongly assuming that the channel flow is fully developed. For small gaps, the bias error is limited but the higher uncertainty on both $\bar{\lambda}$ and w_B propagates so that the flow rate is only known within $\pm 7\%$. In hindsight, M1 is a promising method; though it would have been more profitable for small gap widths, had we measured more locations both with gauge blocks and LDA (in order to decrease uncertainty on $\bar{\lambda}$ and w_B respectively).

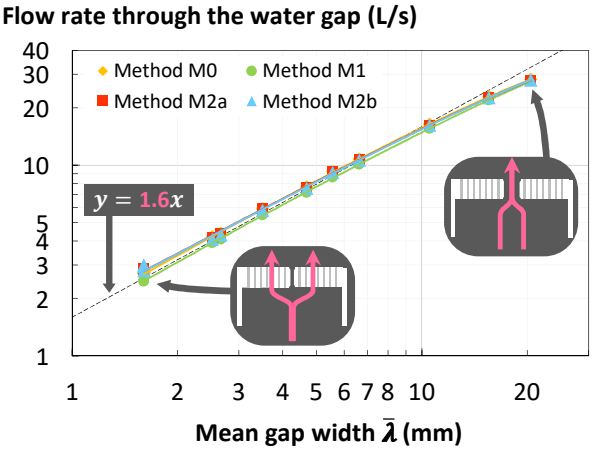

Fig. 12 Illustration of methods **(a)** M2a and **(b)** M2b to reconstruct the channel flow near the walls (here for the case $\lambda = 3$ mm)

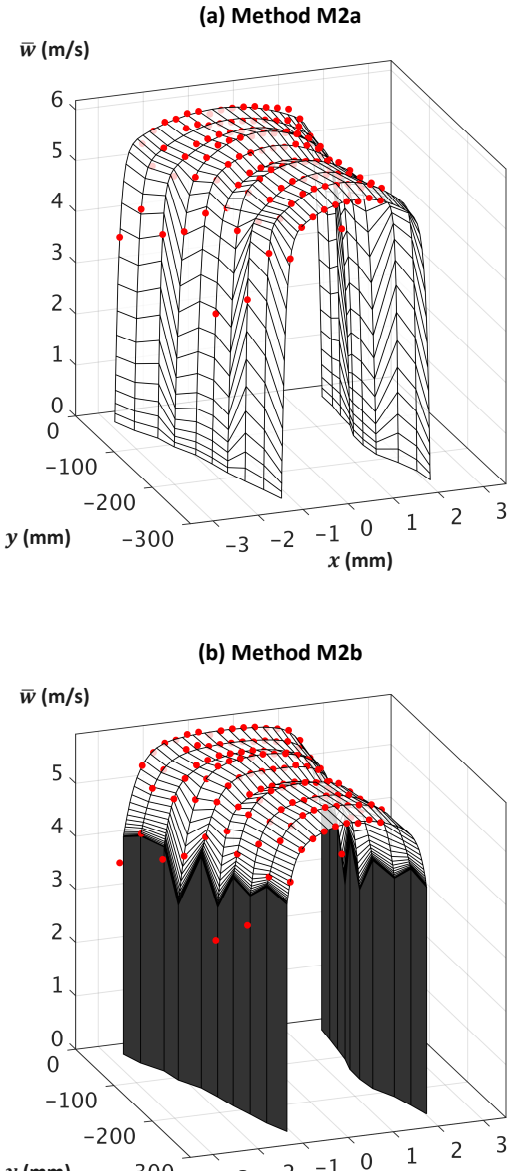

Fig. 11 Illustration of methods **(a)** M2a and **(b)** M2b to reconstruct the channel flow near the walls (here for the case $\lambda = 3$ mm)

The second method also assimilates the water gap to a channel flow. However, we now authorize some variation along the Y-axis. The idea is to fit a separate 2D analytical profile for each line of LDA data parallel to the X-axis (Fig. 11). Logarithmic and power laws both are well-known universal profiles; however, they are not suited to represent the axial velocity from wall to wall because their slope is discontinuous at the channel mid-plane. Moreover, they are designed for fully developed turbulent flows, which, as we said above, is hardly ever observed in our experiments. Instead, we came

up with an analytical model much more focused on the flow rate prediction than on the physical accuracy of the boundary layer. Inspired by the work of Stigler (2016), the i-th approximate profile of axial velocity $\widehat{w}_i(x)$ comprises two adjustable laminar and turbulent components given by Eq. (7):

$$\widehat{w}_i(x) = \beta_3^i \left(1 - \left|\frac{x-\beta_1^i}{\beta_2^i}\right|^2\right) + \beta_4^i \left(1 - \left|\frac{x-\beta_1^i}{\beta_2^i}\right|^{\beta_5^i}\right) \quad (7)$$

where β_1^i and β_2^i are the local center and half-width of the channel respectively, β_3^i and β_4^i are the scaling velocities for the laminar and the turbulent components respectively, and β_5^i is the flatness coefficient of the turbulent part (the larger β_5^i, the flatter the i-th profile). These parameters are optimized for each row of LDA data parallel to the X-axis, thanks to the Trust-Region-Reflective algorithm built in Matlab (advanced nonlinear least-squares, see *e.g.* Vanden Berghen 2004 for a concise description). Two variants of the second method were tested. In the first variant (labeled M2a), the half-width β_2^i was constrained to match the distance λ_i measured by the gauge blocks within the aforementioned tolerance range. Consequently, each approximate profile $\widehat{w}_i(x)$ ends up defined on an interval whose width is precisely equal to λ_i (Fig. 11a). The flow rate per unit length, noted q_i for the i-th location along the Y-axis, is then given by Eq. (8) below:

$$q_i = \frac{4\beta_2^i\beta_3^i}{3} + \frac{2\beta_2^i\beta_4^i\beta_5^i}{\beta_5^i+1} \quad (8)$$

In the second variant (labeled M2b), the β_2^i are left unconstrained. In practice, it always led to β_2^i slightly overestimating the measured half-width $\lambda_i/2$. The optimized profile $\widehat{w}_i(x)$ is cropped afterwards so as to respect the width measured by gauge blocks. This means that the no-slip condition is no longer met at the channel walls (dark vertical trapezoids on Fig. 11b highlight the non-zero velocities at both walls). The closed-form formula for q_i is a bit more convoluted in this case. All the same, for both variants, the trapezoidal rule gives the flow rate Q_B from the linear values q_i.

The main drawback of methods M2a and M2b is that they require at least five data points for each row parallel to the X-axis. As a consequence, these methods could not be used to reconstruct the missing data near the rear window for $\lambda = 1$ mm, as only one or two points were collected there. On the bright side, Eq. (7) was applied to numerical profiles computed by code Cast3M, and the approximate flow rate was within a $\pm 1\%$ for any value of the Reynolds number. Unlike M1 for which the cross-sectional area and bulk velocity in the water gap were prerequisite, M2a and M2b yield the flow rate with no intermediate quantity. Therefore, the uncertainty on the flow rate is lower for M2a and M2b than for M1: around $\pm 2\%$ for large gaps (10 approximate profiles) and $\pm 3\%$ for small gaps (only 5 to 7 profiles for $\lambda = 1$ mm).

As a conclusion, one can look at Fig. 12 for an illustration of the small differences between all four methods introduced in this chapter. The computed flow rates span in a range of about ± 0.5 L/s.

5 Summary of the main results and discussion

The main objective of this experimental campaign was to record the evolution of the flow rate through the water gap, and of the pressure drop across the grid, when the distance between the grids ranges from 1 to 20 mm. The inlet flow rate was kept constant near 120 L/s. Therefore, the flow rate through the half-grids can be derived easily by subtraction.

Fig. 14 sums up all the obtained results within three subplots. Displayed from the top to the bottom of the figure are the flow rates, the bulk velocities and the pressure drops. The circle markers are meant for the measured values, along with plain thick trend lines. For the flow rates and bulk velocities (Fig. 14a and Fig. 14b respectively), the measured values correspond to the average of all outputs produced by methods M0, M1, M2a and M2b. For the pressure drops (Fig. 14c), these are the raw experimental measures. The plain thin lines on Fig. 14 depict the uncertainty ranges. For the flow rates and bulk velocities, these ranges come from the lower and

upper bounds among all the aforementioned methods. For the pressure drop, it is the $\pm 5\%$ uncertainty quoted in section 2.

A second-order polynomial fits the experimental curves of Fig. 14a with an accuracy very much below the uncertainty interval. Actually, the flow rate through the water gap turns out to be almost proportional to the mean gap width $\bar{\lambda}$. Fig. 12 clearly showed that the coefficient of proportionality is greater than 1, which proves that flow redistribution occurs. Indeed, it means that, when the gap widens, more water pours into it than the enlargement explains alone. In other words: when the gap is almost closed, cross-flows are directed from the bypass into the grids, and when the width is being increased, the cross-flow direction progressively reverses, at a constant pace. The flow rate through the grids (also Fig. 14a) follows a curve symmetrical to the one related to the bypass, although the former suffers from more absolute uncertainty than the latter (because of the additional uncertainty put down to the loop flowmeter).

The bulk velocity (Fig. 14b) decreases when the gap grows wider, both inside the gap and the grids. In our case, velocities on either side of the grid "outer strap" are about shifted by 1 m/s; this discontinuity can be challenging for unready numerical schemes. The uncertainty interval on the water gap curve gets bigger as the width $\bar{\lambda}$ decreases, as expected (see section 4).

The pressure drop curve (Fig. 14c) displays a falling trend similar to the bulk velocity. It also exhibits a little more erratic behavior: some of the 13 circle markers on the figure stick out of the global tendancy, uncertainties included. Because each configuration took hours to complete, the tests were carried out on consecutive days. The calibration of the pressure sensors was identical from one test to another; however it appears that the operational conditions were somehow unsettled. The exact reason for such variations remains unknown.

The global consistency of our results was checked by reconstructing the pressure drop from the mock-up coefficient K_G (measured in section 3) and the flow rate through the grids Q_B (measures shown on Fig. 14a), and comparing it with the actual pressure drop measures shown on Fig. 14c. The reconstructed pressure drop across the half-grids was computed with Eq. (9):

$$\widehat{\Delta p}(\bar{\lambda}) = \frac{1}{2}\rho K_G(\bar{\lambda})\left(\frac{Q_G}{A - A_B}\right)^2 \tag{9}$$

The area $A - A_B$ supposedly matches the fraction of the flow which ends up inside the grid holes, namely Q_B. As a reminder, $K_G(\bar{\lambda})$ is the pressure drop

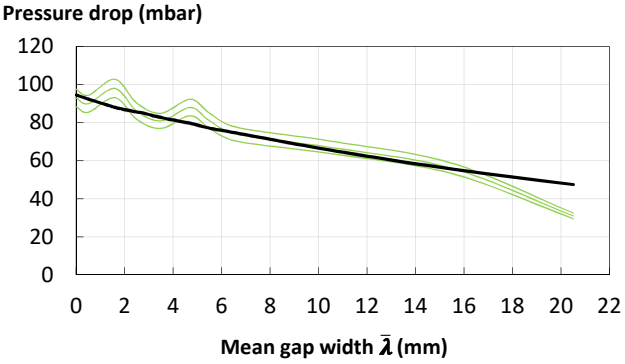

Fig. 13 Consistency of the various measures of the DIVA+G campaign (— Experimental measures of Δp; — Reconstruction of Δp from measures or $\bar{\lambda}$, $K_{\bar{\lambda}}$ and Q_B)

coefficient of the half-grids, which decreases linearly along with $\bar{\lambda}$ according to Eq. (5). Fig. 13 demonstrates the global reliability of the data produced by this experimental campaign. The results gathered with a fully closed gap ($\bar{\lambda} = 0$; see section 3) were included in the graphic.

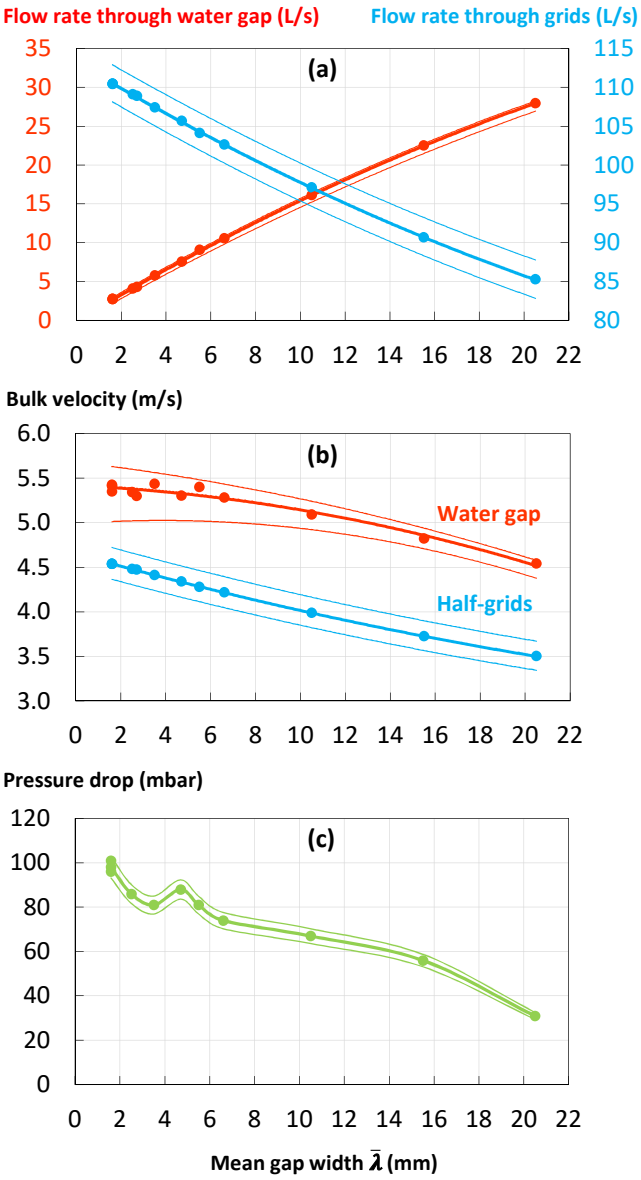

Fig. 14 Experimental results in terms of **(a)** flow rates, **(b)** bulk velocities and **(c)** pressure drop; measures are indicated by circle markers; trend lines are plotted as thick lines; uncertainty ranges are plotted as thin lines

Ultimately, we compared our experimental results to the analytical model proposed by de Lambert et al. (2020), which consists in a hydraulic network with properly designed resistance coefficients. Because rods were not included in the mock-up, the so-called "Model 2" was the most adequate (no resistance to redistribution cross-flows). As shown by Fig. 15, the agreement is quite good, with discrepancies mainly comprised inside the uncertainty interval (except for the widest gap).

Such models sometimes require more insight as to how the redistribution occurs. More specifically, one

Fig. 16 Vertical LDA plane at $y = -27$ mm, built from around 450 measures of the X- and Z-component of the mean velocity. Streamlines are represented in faint lines. Vectors and profiles are plotted at regular heights

can wonder about the distance upstream of the grid where the cross-flows initiate, or how many fuel rods are affected. Fig. 16 may help answer qualitatively to these questions. It is a visualization of more than 450 LDA measures taken in the vertical plane at $y = -27$ mm. Both X- and Z-component were collected in successive tests. The local gap width was about 3.7 mm. A dozen locations were probed only 1 mm upstream of the half-grids ($z = -41$ mm). Some of these LDA measures were successful for the X-component solely, hence they are not represented on Fig. 16. Likewise, about 20 points were collected just 2 mm downstream of the half-grids ($z = 2$ mm). We can see that the flow loses uniformity less than 1 cm before hitting the bottom face of the holed plate, and that it returns to a flat profile after a distance similar to the holes plates height L_Z. For this configuration, cross-flows upstream of the bypass seem to spread over about 1 cm on each side.

6 Conclusions

An experimental campaign was conducted in order to observe the water flow behavior when crossing grid-like devices separated by an adjustable gap. Two

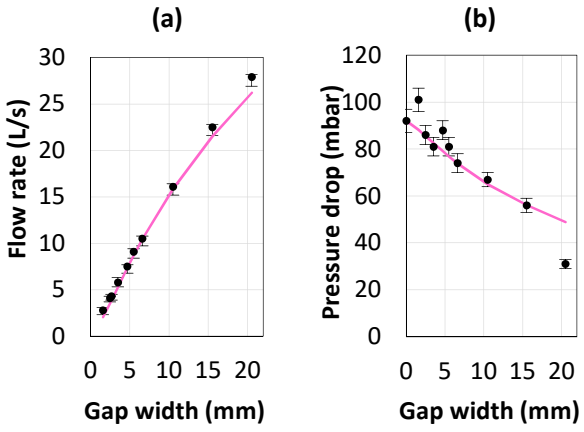

Fig. 15 Comparison between the DIVA+G experimental measures and the analytical model of de Lambert et al. (2020) in terms of **(a)** flow rate through the water gap and **(b)** pressure drop (● Experimental values with uncertainty range; — Analytical model [model 2])

generic mock-up half-grids were 3D printed in plastic material. The manufacturing limited quality was circumvented by thorough measures of the cross-sectional area and pressure drop coefficient of the printed parts. The flow rate between the grids was determined using different advanced methods, all making use of hundreds of LDA acquisitions of the mean axial velocity in the water gap. We found that the flow rate and the gap width are almost proportional. The coefficient of proportionality is greater than one, revealing the progressive change in the flow preferential path: through the grids for small widths, through the gap for large widths. A full field visualization shown that this so-called redistribution effect initiated at a very small distance upstream of the obstacle, and did not spread laterally farther than one or two rows of holes. The consistency of the experimental results was cross-checked internally and then confronted to an analytical model available in the literature, achieving very good agreement. Our raw measures and post-processings are downloadable on Figshare by anyone in need of reference data concerning the flow redistribution across grids (see references).

References

Andersson T, Almberger J, Björnkvist L (2005) A decade of assembly bow management at Ringhals. Structural Behaviour of Fuel Assemblies for Water Cooled Reactors, IAEA-TECDOC-1454, Vienna, Austria

Anselmet F, Ternat F, Amielh M, Boiron O, Boyer P, Pietri L (2009) Axial development of the mean flow in the entrance region of turbulent pipe and duct flows. C R Mecanique 337(8) 573-584. https://doi.org/10.1016/j.crme.2009.07.001

Cardolaccia J., de Lambert S. (2020) DIVA+G experimental results. Figshare dataset. http://doi.org/10.6084/m9.figshare.12624638

Cast3M website. French Alternative Energies and Atomic Energy Commission. http://www-cast3m.cea.fr/. Accessed 14 May 2020

Coppolani P, Hassenboelher N, Joseph J, Petetrot JF, Py JP, Zampa JS (2004) La chaudière des réacteurs à eau sous pression. Génie Atomique Collection, EDP Sciences, Les Ulis, France

de Lambert S, Campioni G, Faucher F, Leturcq B, Cardolaccia J (2020) Semi-analytical modeling of the flow redistribution upstream from the mixing grids in a context of nuclear fuel assembly bowing. Nucl Eng Des (In Press)

Dean RB (1978) Reynolds Number Dependence of Skin Friction and Other Bulk Flow Variables in Two-Dimensional Rectangular Duct Flow. J Fluids Eng 100(2): 215-223. https://doi.org/10.1115/1.3448633

Fetterman RJ, Franceschini F (2008) Analysis of PWR assembly bow. In: Proc Int Conf PHYSOR'08, Interlaken, Switzerland

Fournier Y, Vurpillot C, Béchaud C (2007) Evaluation of fluid flow in the lower core of a PWR with Code_Saturne. Nucl Eng Des 237: 1729-1744. https://doi.org/10.1016/j.nucengdes.2007.02.025

Framatome (2018) GAIA Fuel Assembly. Designed for Reliability, Robustness and Performance. https://www.framatome.com/EN/customer-2836/gaia-fuel-assembly-reliability-robustness-performance.html. Accessed 14 May 2020

Gabrielsson P, Schrire D, Suvdantsetseg E (2018) Investigation of the Development of Fuel Assembly Bow in Ringhals 3 and 4. In: Proc Int Conf Top Fuel'18, Prague, Czech Republic

Horváth A, Dressel B (2013) On numerical simulation of fuel assembly bow in pressurized water reactors. Nucl Eng Des 265: 814-825. https://doi.org/10.1016/j.nucengdes.2013.09.031

IAEA (2010) Review of Fuel Failures in Water Cooled Reactors. IAEA Nuclear Energy Series, IAEA, Vienna, Austria

Idel'cik IE (1986) Mémento des pertes de charge (3ème édition). Collection Direction des études et recherches d'Electricité de France, Eyrolles, Paris, France

IRSN (2012) Le point de vue de l'IRSN sur la sûreté et la radioprotection du parc électronucléaire français en 2010. Rapport DSR N°466, IRSN, Fontenay-aux-Roses, France

IRSN (2017) Critères de tenue du combustible des réacteurs à eau sous pression. Avis IRSN/2017-00168, IRSN, Fontenay-aux-Roses, France

Karlsson L, Manngård T (1999) Modelling of PWR Fuel Assembly Deformations During Irradiation. In: Proc Int Conf SMiRT'15, Seoul, South Korea

Karoutas Z, Lang K, Joffre P, Baglietto E, Brewster R, Volpenhein E (2010). Evaluating PWR Fuel Performance Using Vessel CFD Analysis. In: Proceedings of Top Fuel'10, Orlando, USA

Lascar C, Champigny J, Chazot B, Goreaud N, Méry de Montigny E, Pacull J, Salaün H (2015) Advanced predictive tool for fuel assembly bow based on a 3D coupled FSI approach. In: Proc Int Conf Top Fuel'15, Zurich, Switzerland

McLaughlin DK, Tiederman WG (1973). Biasing correction for individual realization of laser anemometer measurements in turbulent flows. Phys. Fluids 16 (12), 2082. https://doi.org/10.1063/1.1694269

Ricciardi G, Boccaccio E (2015) Modelling of the flow induced stiffness of a PWR fuel assembly. Nucl Eng Des 282: 8-14. https://doi.org/10.1016/j.nucengdes.2014.11.027

Stabel J, Dressel B, Marx V, Muench CJ, Horvath A, Brun C, Méry de Montigny E, Song C (2011) Advanced methodology to predict in-reactor bow of PWR fuel assemblies for efficient design optimization: background, validation, examples. In: Proc Water React Fuel Perform Meet'11, Chengdu, China

Stigler J (2016) Contribution to investigation of turbulent mean-flow velocity profile in pipe of circular cross-section. In: AIP Conf Proc 1768, 020010. https://doi.org/10.1063/1.4963032

Vanden Berghen F (2004) Trust Region Algorithms. http://www.applied-mathematics.net/optimization/optimizationIntro.html. Accessed 14 May 2020

Wanninger A, Seidl M, Macián-Juan R (2018) Mechanical analysis of the bow deformation of a row of fuel assemblies in a PWR core. Nucl Eng Technol 50(2): 297-305. https://doi.org/10.1016/j.net.2017.12.009

Xu Y, Conner M, Yuan K, Dzodzo MB, Karoutas Z, Beltz SA, Ray S, Bissett TA, Chieng CC, Kao MT, Wu CY (2012) Study of impact of the AP1000 reactor vessel upper internals design on fuel performance. Nucl Eng Des 252: 128-134. https://doi.org/10.1016/j.nucengdes.2012.06.036